Microstructural Analysis of a C/SiC Ceramic Based on the Segmentation of X-ray Phase Contrast Tomographic Data

Oliver Wirjadi[a*] Alexander Rack[b] André Liebscher[c]
Jürgen Meinhardt[d] Katja Schladitz[a] Behrang Shafei[a,c]
Gabriele Steidl[c]

[a]Fraunhofer ITWM, Kaiserslautern, Germany
[b]European Synchrotron Radiation Facility, Grenoble, France
[c]University of Kaiserslautern, Kaiserslautern, Germany
[d]Fraunhofer ISC, Würzburg, Germany

September 30, 2013

Keywords: Micro-structure; Microtomography; X-ray Phase Contrast; Synchrotron Radiation

Abstract

Our work copes with the analysis of 3D data of carbon fiber reinforced silicon carbide ceramics (C/SiC). In the production process of C/SiC, a porous carbon preform reinforced with bundles of carbon fibers is infiltrated with liquid silicon at approximately 1500° C. The reaction between

*Correspondence address: Dr. Oliver Wirjadi, Fraunhofer ITWM, Fraunhofer-Platz 1, D-67663 Kaiserslautern, Tel.: +49-(0)631-31600-4625, e-mail: oliver.wirjadi@itwm.fraunhofer.de

liquid silicon and carbon creates a layer of silicon carbide (SiC) while the silicon vanishes almost completely. This material is able to withstand extremely high temperatures and it is extremely tough with respect to fracture. To increase the efficiency of the costly and time consuming production process, the development of methods for monitoring the quality of the material is helpful. For instance, the thickness of the SiC layer is a valuable measure. Moreover, due to different coefficients of thermal expansion of the components typically cracks appear during the production process. For effective analysis the availability of 3D high resolution image data is necessary that can be acquired by synchrotron-CT. In a first image processing step, we segment the 3D image data (C/SiC) with a convex optimization approach incorporating spatial regularity. Further, we work on the detection of cracks using an eigenvalue analysis of the 3D Hessian matrix determined in each pixel.

1 Introduction

Scanning electron microscopy (SEM) as well as hard X-ray microtomography are well established techniques in materials research with complementary characteristics. Using electrons as probe for imaging allows one to reach highest spatial resolutions for imaging in combination with analytical techniques but commonly restricted to two-dimensional images. X-ray microtomography gives access to volume images in a widely non-destructive manner but commonly is not an analytical technique with comparably limited sensitivity. In this paper we shall outline how hard X-ray phase contrast can partially be used to bridge the gap between the two techniques: while the common absorption contrast in X-ray imaging allows one to visualize density changes, X-ray phase contrast is a modality which exploits electron density variations in the sample. Hence, a contrast which is similar to the SEM contrast is accessible in a three-dimensional manner [1]. Consequently, combining both techniques offers a powerful approach to study weakly contrasted multi-constituent samples in a quantitative manner which opens quantitative volume image analysis to a new range of specimens.

As an example application fiber reinforced ceramic composites were chosen due to their wide-spread use: carbon fiber reinforced silicon carbide ceramics (C/SiC) are applied for example as brake or clutch disks. Here, short fiber bundles are used instead of individual fibers. These bundles consisting of several hundreds of fibers increase the fracture toughness of the ceramic. A special case are short fiber bundles distributed isotropically within a plane. In the production process of these ceramics, a porous carbon preform reinforced with bundles of carbon fibers (C/C) is infiltrated with liquid silicon at approximately 1 500°C. The reaction between liquid silicon and carbon creates a layer of silicon carbide (SiC) while the silicon vanishes almost completely. The materials properties of the resulting C/SiC ceramic are determined by the complex 3D network of

carbon fiber bundles, silicon, and SiC ceramic. In particular, this material is able to withstand extremely high temperatures and it is extremely tough with respect to fracture. For classical X-ray imaging, these kind of samples represent a challenge as carbon fibres show poor contrast due to their homogeneous density while furthermore the density changes between Si and SiC are poor as well.

Usual quantitative analysis based on 2D images as arising from scanning electron microscopy can capture the volume fractions of the components and to some extent the thickness of the SiC layer. However, valuable 3D information is missing. We used the SEM images here as an analytical probe, i. e. to identify the material phases in the phase- contrast volume tomographic data due to their morphology in comparison with the SEM images [2]. Consequently, micro computed tomography (μCT) was used to acquire high resolution 3D image data enabling the spatial analysis of the SiC layer of about 20μm thickness, see Figure 1. Using synchrotron radiation (SRμCT) and the associated inline X-ray phase contrast results in an image quality also allowing to analyze the remaining porosity as well as the network of micro-cracks arising from different coefficients of thermal expansion of the components and being typical for C/SiC ceramics.

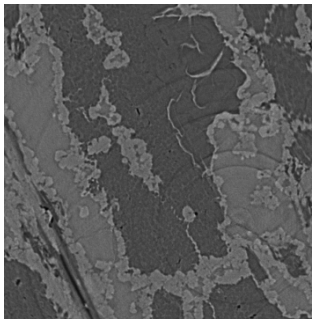

Figure 1: One slice from a 3D image of a C/SiC sample acquired at the BAM*line* at BESSY [3].

Quantitative geometric analysis [6] requires segmentation of the components of the C/SiC-microstructure. Thus we first segment the carbon, silicon carbide, and pore space components applying a recently developed method [4] that exploits the fact that Si and C react to form the SiC layer. The new segmentation method is based on convex optimization incorporating spatial regularity. Subsequently, the volume fractions of carbon matrix, carbon fibers, and silicon carbide can be measured.

Local shape analysis [5] bears the potential to detect micro-cracks and to analyze the intrinsic fiber structure of the C component. Thus, second, we use this approach on the original unsegmented gray value image to find micro-cracks. It is based on an eigenvalue analysis of the Hessian matrix in each pixel. Morphological post-processing yields the micro-cracks.

Combining the geometric information gained from these two independent methods, renders detailed statements about the spatial arrangement possible. As an example, we show that the micro-cracks cross all three solid components.

The tomographic technique used is shortly described in the following Section 2, followed by a summary of the segmentation method in Section 3. Then, the method for detecting cracks based on a local shape analysis is introduced in Section 4. The analysis methods are shortly introduced in Section 5. Finally, Section 6 shows exemplary results and identifies tasks for further research.

2 Synchrotron-based Microtomography

The tomographic volume image analyzed within this article was acquired at the microtomography facility of the BAM*line* (BESSY II synchrotron light source, Helmholtz-Zentrum Berlin, Germany) [3].

For the data acquisition an X-ray photon energy of 17 keV was selected via the beamline's double-multilayer monochromator. High-resolution X-ray images

were acquired using an indirect detector consisting of a 40-µm thick $CdWO_4$ single-crystal scintillator glued on top of an undoped $Y_3Al_5O_{12}$ substrate: the resulting luminescence image is projected by an inhouse-designed optical system (macroscope, 9× nominal magnification, 0.5 numerical aperture of the front objective) on the CCD chip of a Princeton Instruments camera (type: VersArray: 2048B) [3]. Parasitic luminescence from the substrate is blocked by a glass filter placed downstream the objective. The resulting effective pixel size is 1.5 µm, a spatial resolution of <4 µm was measured via a line-spread function. The resulting detector field-of-view is approximately 3 mm × 3 mm.

1 500 projection images were acquired over a tomographic scan range of 180 degree. Tomographic reconstruction was performed using the filtered backprojection algorithm via the software package PyHST of the European Synchrotron Radiation Facility. A propagation distance of 27 mm between the sample and the detector (scintillator) was chosen in order to increase the contrast by means of X-ray inline phase contrast [7]. Exploiting the full refractive index of the specimen for contrast increases drastically the sensitivity, i. e. while the attenuation signal is related to the physical density of the material, X-ray phase contrast is proportional to the election density. Hence, X-ray phase contrast images can reveal an image sensitivity similar to electron microscopy [8].

A typical sample slice of the data set acquired is displayed in Figure 1. The three main phases Si, C and SiC can be visually identified. This interpretation of the grayscaled SμCT image has been verified: a scanning electron microscopy image of a similar sample was compared with a tomographic slice employing inline X-ray phase contrast [2]: the different material phases were identified using electron backscatter techniques. Due to the similar morphology as well as arrangement of the different constituents in both images one can consider the interpretation of the SμCT volume data set as correct.

3 Segmentation

Image segmentation always suffers from uncertainty in defining the structures which are to be characterized. Therefore, it is desirable to incorporate prior or expert knowledge into the design of specialized segmentation routines. This section briefly reviews the segmentation model adapted to volumetric 3D images of C/SiC introduced by [4]. This model allows to exploit the fact, that Si and carbon are always separated by the SiC layer.

We work with grayscale images $F : \{1, \dots, n_1\} \times \{1, \dots, n_2\} \times \{1, \dots, n_3\} \to \mathbb{R}$ defined on a discrete grid and often reshaped to $f : \{1, \dots, N\} \to \mathbb{R}$ where $N = n_1 n_2 n_3$ denotes the number of pixels.

To obtain the vector of characteristic functions of the segments

$$u = (u_k)_{k=1}^{c},\ u_k = (u_k(j))_{j=1}^{N} \in \mathbb{R}^N$$

one can solve

$$\operatorname*{argmin}_{u \in \mathbb{R}^{cN}} \sum_{k=1}^{c} \sum_{j=1}^{N} u_k(j) s_k(j) + \lambda \sum_{k=1}^{c} \mathrm{TV}(u_k) \tag{1}$$

$$\text{s.t. } u_k(j) \in \{0, 1\}, \quad \sum_{k} u_k(j) = 1 \tag{2}$$

where c is the fixed number of classes, $\lambda \in \mathbb{R}$ a fixed regularization parameter, and the constant $s_k(j)$ determines a dissimilarity between cluster k and pixel j. For instance, $s_k(j) := |r_k - f(j)|$ where r_k is a prototypical gray-value of segment k to be determined beforehand (also called center).

$\mathrm{TV} : \mathbb{R}^N \to \mathbb{R}$ denotes the discrete total variation where $\mathrm{TV}(u_k)$ corresponds to the length of the boundary of segment k as long as u is binary. The total variation has been introduced by [9] for image processing applications. In particular, there exist many applications to labeling and segmentation, see the

references in [4]. Moreover, the total variation has been applied to the segmentation of 3D CT-images of multifilament superconductors [10]. In the following, we introduce a discrete variant of the total variation using forward differences. Using the forward difference matrix

$$D_n := \begin{pmatrix} -1 & 1 & & & \\ & -1 & 1 & & \\ & & \ddots & \ddots & \\ & & & -1 & 1 \\ 0 & & \dots & & 0 \end{pmatrix} \in \mathbb{R}^{n \times n} \tag{3}$$

with mirrored (Neumann) boundary conditions, we obtain the discrete gradient

$$\begin{pmatrix} f_x \\ f_y \\ f_z \end{pmatrix} = \underbrace{\begin{pmatrix} I_{n_3} \otimes I_{n_2} \otimes D_{n_1} \\ I_{n_3} \otimes D_{n_2} \otimes I_{n_1} \\ D_{n_3} \otimes I_{n_2} \otimes I_{n_1} \end{pmatrix}}_{D} f. \tag{4}$$

Thereby, $\otimes$ denotes the Kronecker-product, i.e.,

$$A \otimes B := \begin{pmatrix} a_{11}B & \dots & a_{1n_2}B \\ \vdots & \ddots & \vdots \\ a_{n_1 1}B & \dots & a_{n_1 n_2}B \end{pmatrix} \in \mathbb{R}^{m_1 n_1 \times m_2 n_2}$$

with $A \in \mathbb{R}^{n_1 \times n_2}$ and $B \in \mathbb{R}^{m_1 \times m_2}$. Using the notation $\|x\|_{2,1} := \sum_{j=1}^{N} \sqrt{x_j^2 + x_{N+j}^2 + x_{2N+j}^2}$ for $x \in \mathbb{R}^{3N}$, the discrete total variation for images $f : \{1, \dots, N\} \to \mathbb{R}$ is defined by

$$\mathrm{TV}(f) := \|Df\|_{2,1} = \sum_{j=1}^{N} \|(Df)(j)\|_2 = \sum_{j=1}^{N} \sqrt{f_x(j)^2 + f_y(j)^2 + f_z(j)^2}. \tag{5}$$

The total variation enforces neighboring pixels to be in the same pixel while respecting edges in the image in contrast to the quadratic regularization term $\|Df\|_{2,1}^2$.

3.1 Optimization Algorithms

The optimization over the characteristic vectors of the segments $u \in \{0,1\}^{cN}$ in (1) is NP-hard. Hence, we relax the binary constraint to $u_k(j) \in [0,1]$ and obtain the continuous and convex optimization problem

$$\operatorname*{argmin}_{u \in \mathbb{R}^{cN}} \sum_{k=1}^{c} \sum_{j=1}^{N} u_k(j) s_k(j) + \lambda \sum_{k=1}^{c} \mathrm{TV}(u_k) \tag{6}$$

$$\text{s.t. } u_k(j) \in [0,1], \quad \sum_k u_k(j) = 1 \tag{7}$$

as an approximation of (1).

To minimize (6), we use the *alternating direction method of multipliers* that is equivalent to the Douglas-Rachford splitting applied to the dual problem, see, e.g., [11, 12]. In fact, we have to solve a sequence of simpler subproblems that update the primal and the dual variables of our optimization problem. This is explained in detail in [4, 10].

3.2 Respecting Separating Layers in the Segmentation Model

Since the C/SiC ceramics have the property that the carbon pre-form and the carbon fiber layers are separated by silicon carbide, we adapt our segmentation model to respect this property in terms of the dissimilarity constant s.

We want to forbid pixels of non-touching segments to be neighbors. There-

fore, we introduce for every pixel the binary distance function

$$b_k : \{1, \dots, c\} \to \{0, 1\},\ b_k(k') := \begin{cases} 1 & \text{if segment } k' \text{ must not touch segment } k \\ 0 & \text{otherwise.} \end{cases} \tag{8}$$

The definition of b determines which segments are allowed to have common boundary. Moreover, we need an initial segmentation $l_0 : \{1, \dots, N\} \to \{1, \dots, c\}$ to define

$$P_k(j) := \sum_{i \in \mathcal{N}(j)} b_k(l_0(i)), \quad j = 1, \dots, N,\ k = 1, \dots, c \tag{9}$$

where $\mathcal{N}_j$ denotes the eight-neighborhood of pixel j. With this penalizing function at hand and a new regularization parameter $\mu \geq 0$, we set

$$s_k(j) := |f(j) - r_k| + \mu P_k(j). \tag{10}$$

This yields a two-step approach:

1. Compute an initial segmentation l_0 by solving (6) with $s_k(j) := |r_k - f(j)|$.
2. Change s to $s_k(j) := |f(j) - r_k| + \mu P_k(j)$ and compute the final segmentation by solving (6) again with the amended constant s.

4 Crack detection

To find micro cracks we follow [5] using the method for detecting closed cell windows in open cell foams from [13, 14] and extending a filter originally introduced to enhance blood vessels in μCT images [15]. It can be formalized as follows:

Denote by $g\colon \mathbb{R}^3 \mapsto \mathbb{R}$ the continuous extension of image F and by $G(x,s)$ the isotropic Gaussian kernel with standard deviation s. Then following [16, 17] the γ-normalized derivative of g at scale s is given by

$$\frac{\partial}{\partial x} g_s(x) = s^\gamma g(x) * \frac{\partial}{\partial x} G(x,s)\,, \tag{11}$$

where $\gamma \in [0,1]$ is a normalization factor that ensures the invariance of the derivative across different scales. As crack detection is related to ridge detection (the maximal filter response is expected at the centre of the structure) we use $\gamma = 0.75$ as suggested in [17].

The idea is now to use the Gaussian kernel as a probe to account for the second order structure of g. More precisely, we study the contrast variation in the region $(-s,s)$ around a point x by evaluating the second order partial derivatives given by the Hessian matrix $H(x,s)$. Geometrically H maps the spherical neighbourhood centered at x to an ellipsoid that fits the strength of local contrast variation. Its semi-axes correspond to the eigenvectors of H. Hence, the local geometric structure of the image can be determined by the ratio of their lengths, that is, the eigenvalues of H.

Denote by λ_i $(i = 1,2,3)$ the eigenvalues of H ordered such that $|\lambda_1| < |\lambda_2| < |\lambda_3|$. Then detecting lamellar micro cracks corresponds to searching for prolate ellipsoids with λ_1 and λ_2 small while λ_3 is significantly larger. This means searching for points x for which the ratio of the second and the largest eigenvalue vanishes, i.e.

$$R_{\mathrm{A}}(x,s) = |\lambda_2|/|\lambda_3| \to 0\,. \tag{12}$$

To stabilize the filter response we take into account two additional features: As the ellipse that corresponds to a crack should differ from a sphere, i.e. a

blob-like structure, the ratio

$$R_{\mathrm{B}}(x,s) = \frac{A_{\mathrm{circle}(\lambda_1)}}{A_{\mathrm{ellipse}(\lambda_2,\lambda_3)}} = \frac{|\lambda_1(x,s)|}{\sqrt{|\lambda_2(x,s)\lambda_3(x,s)|}} \tag{13}$$

should vanish. Here $A_{\mathrm{circle}(\lambda_1)}$ denotes the area of the circle defined by λ_1 and $A_{\mathrm{ellipse}(\lambda_2,\lambda_3)}$ is the area of the largest cross-sectional ellipse that is orthogonal to the circle defined by λ_1. Moreover, to prevent unpredictable filter responses due to random noise in the background the squared sum of the eigenvalues of the Hessian H

$$N_{\mathrm{F}}(x,s) = \left(\sum_{i=1}^{3} \lambda_i(x,s)^2\right)^{1/2} \tag{14}$$

should not vanish at x.

To obtain a filter that enhances cracks we combine the quantities given in (12)–(14) into a product of scaled exponentials of R_A, R_B and $1 - N_F$. The resulting measure $W(x,s)$ attains its maximum for cracks with size proportional to s. As the size is usually not known in advance we search the maximal response over several scales $s_{\min}, s_{\max} \in \mathbb{R}_+$ yielding the filter $W(x) = \max_{s_{\min} \le s \le s_{\max}} W(x,s)$.

This filtering w. r. t. locally lamellar structures yields the micro cracks but many other parts of the structure, too. In particular the filter enhances the interface between the components C and SiC. Excessive post-processing applying morphological transforms, orientation analysis, and object filtering w. r. t. volume and shape allows nevertheless to separate the cracks from these erroneously detected regions thus enabling further characterization of the cracks.

5 Quantitative analysis

The intrinsic volumes – the volume V, the surface area S, the integral of mean curvature M and the Euler number χ form a basic set of geometric character-

istics that can be measured efficiently from 3D image data [6, Chapter 5]. For a convex object, M is up to a constant the mean width. The Euler number is a topological characteristic alternately counting the connected components, the tunnels, and the holes of the particle. For a convex body, we have $\chi = 1$, for a torus $\chi = 1 - 1 = 0$, and for a sphere $\chi = 1 + 1 = 2$.

For components of macroscopically homogeneous micro-structures that do not feature a natural object structure, the densities of the intrinsic volumes are more suitable. Instead of the absolute values of these four functionals, now their ratio to the sample volume is considered: the volume fraction V_V, the specific surface area S_V, and the densities of the integral of mean curvature M_V and the Euler number χ_V. A shape factor can be derived from these, too. The so-called structure model index originally introduced to evaluate bone structure [18] takes values 4, 3, and 0 for ideal systems of non-overlapping balls, cylinders, and planes, respectively. It can be derived from the densities of the intrinsic volumes $4\pi V_V M_V / S_V^2$ and therefore as these quantities be estimated from image data without a surface meshing [19].

6 Results & Conclusions

C/SiC materials behave anisotropically due to the anisotropic orientation of the short fiber bundles. Roughly speaking, besides carbon (matrix and fibers), silicon, and silicon carbide, the micro-cracks form a fourth phase that is typical for this material. They arise from the different thermal expansions of carbon fibers and silicon/silicon carbide matrix and extend from fiber bundle to fiber bundle, orthogonal to the fiber bundle orientation. Thus the micro-cracks are anisotropically oriented, too. Segmentation of both the micro-cracks as well as the SiC component opens the opportunity to correlate geometric characteristics of these components with macroscopic materials properties. In particular, oxi-

dation of the carbon fiber bundles mainly spreads through the fiber bundles but the micro-cracks act as diffusion paths for oxide, too.

The segmentations achieved so far reveal the micro-cracks and show that they cross all solid micro-structure components. However, the segmentation of the micro-cracks relies on heavy morphological post-processing preventing subsequent quantitative analysis of the crack structure. Analysis e. g. of orientation, local thickness, or connectivity of the crack structure requires a segmentation that better preserves the original structure. This in turn needs higher resolution as well as stronger gray value contrast. Nevertheless, based on the

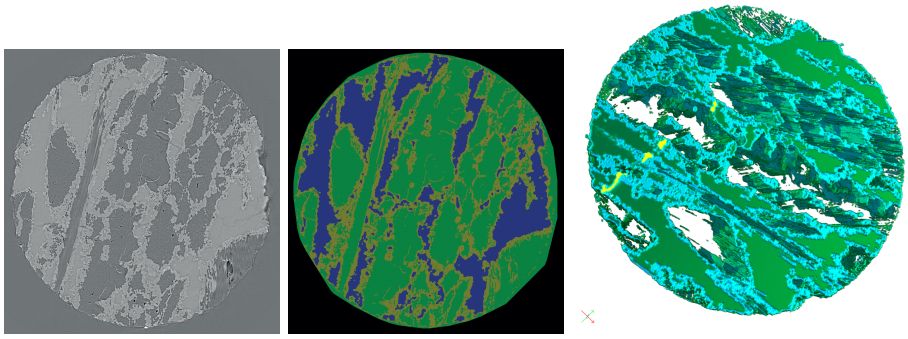

(a) Slice through original (b) Slice through segmentation result (c) Volume rendering with crack

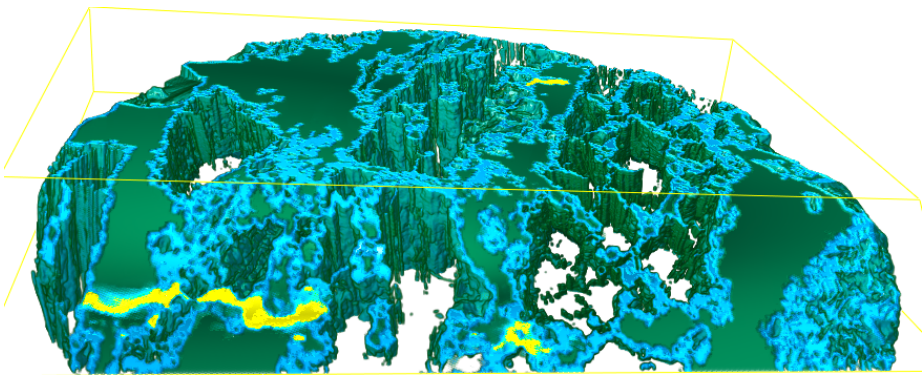

(d) Volume rendering with crack

Figure 2: Segmentation result, 2D slices: blue - Si, green - C, yellow - SiC, volume renderings: lightblue - SiC, green - C, yellow - microcrack.

phase	V_V	S_V
C	47.83 %	57.7 mm^{-1}
Si	25.55 %	20.5 mm^{-1}
SiC	26.65 %	74.0 mm^{-1}

Table 1: Volume density (V_V) and specific surface (S_V) for each of the three microstructural components of the C/SiC.

segmentation derived in 3.1, quantitative analysis of C, SiC, and pore space is possible. Table 1 shows as exemplary results the volume fractions and specific surface areas of the three segmented components. Another practically significant question is to which extent the silicon carbide actually enwraps the carbon fiber bundles. The SiC acts as an oxidation barrier. Thus, no additional oxidation protection is needed if the SiC layer is really intact as the only remaining paths for oxidation would be the micro-cracks that close due to thermal expansion when heated to a couple of 100°C. Obviously, this question can not be answered based on the segmentation from Sec. 3.1, as this relies on the fact that C and pore space pixel are always separated by an SiC layer. More generally, the problem can not be solved based on the given image data, see Figure 3. A

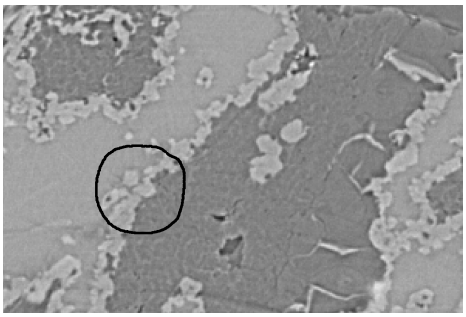

Figure 3: Strongly enlarged subwindow of the SRμCT data set from Figure 1. Given the present lateral resolution, it is impossible to decide whether the SiC layer is completely closed in the center of the indicated region.

satisfactory solution of this question calls for both higher lateral resolution in the 3D data as well as an alteration of the segmentation method, a subject of

ongoing research.

The authors acknowledge support by the German Federal Ministry of Education and Research through project 05M2013 (AniS).

References

[1] Simon Zabler, Peter Cloetens, and Paul Zaslansky. Fresnel-propagated submicrometer x-ray imaging of water-immersed tooth dentin. *Opt. Lett.*, 32(20):2987–2989, 2007.

[2] P.-A. Douissard, A. Cecilia, X. Rochet, X. Chapel, T. Martin, T. van de Kamp, L. Helfen, T. Baumbach, L. Luquot, X. Xiao, J. Meinhardt, and A. Rack. A versatile indirect detector design for hard x-ray microimaging. *J. Instrum.*, 9(7):P09016, 2012.

[3] A. Rack, S. Zabler, B. R. Müller, H. Riesemeier, G. Weidemann, A. Lange, J. Goebbels, M. Hentschel, and W. Görner. High resolution synchrotron-based radiography and tomography using hard X-rays at the BAMline (BESSY II). *Nuclear Instruments and Methods in Physics Research Section A: Accelerators, Spectrometers, Detectors and Associated Equipment*, 586(2):327–344, 2008.

[4] B. Shafei and G. Steidl. Segmentation of images with separating layers by fuzzy c-means and convex optimization. *Journal of Visual Communication and Image Representation*, 23(4):611–621, 2012.

[5] R. Stoessel, O. Wirjadi, M. Godehardt, A. Schlachter, and A. Liebscher. Analysis of inner fracture surfaces in CFRP based on μ-ct image data. In *Conference on Industrial Computed Tomography*. Upper Austrian University of Applied Sciences Wels, 2012. accepted.

[6] J. Ohser and K. Schladitz. *3d Images of Materials Structures – Processing and Analysis*. Wiley VCH, Weinheim, 2009.

[7] P. Cloetens, R. Barrett, J. Baruchel, J.-P. Guigay, and M. Schlenker. Phase

objects in synchrotron radiation hard x-ray imaging. *J. Phys. D*, 29(1):133–146, 1996.

[8] S. Zabler, H. Riesemeier, P. Fratzl, and P. Zaslansky. Fresnel-propagated imaging for the study of human tooth dentin by partially coherent x-ray tomography. *Opt. Express*, 14(19):8584–8597, Sep 2006.

[9] L. Rudin, S. Osher, and E. Fatemi. Nonlinear total variation based noise removal algorithms. *Physica D*, 60:259–268, 1992.

[10] Behrang Shafei. *Multi-Class Image Segmentation via Convex and Biconvex Optimization*. PhD thesis, Kaiserslautern University of Technology, 2013.

[11] J. Eckstein and D. P. Bertsekas. On the Douglas-Rachford splitting method and the proximal point algorithm for maximal monotone operators. *Mathematical Programming*, 55:293–318, 1992.

[12] S. Setzer. Operator splittings, Bregman methods and frame shrinkage in image processing. *International Journal of Computer Vision*, 92(3):265–280, 2011.

[13] J. Kampf, A. Liebscher, and C. Redenbach. Segmentation and statistical analysis of the wall system in ceramic foams. In preparation., 2013.

[14] A. Liebscher. *Stochastic Modelling of Foams*. PhD thesis, Fachbereich Mathematik, TU Kaiserslautern, 2013.

[15] A. Frangi, W. Niessen, K. Vincken, and M. Viergever. Multiscale vessel enhancement filtering. In W. Wells, A. Colchester, and S. Delp, editors, *Medical Image Computing and Computer-Assisted Interventation MICCAI98*, volume 1496 of *Lecture Notes in Computer Science*, pages 130–137. Springer, 1998.

[16] T. Lindberg. Feature detection with automatic scale selection. *International Journal of Computer Vision*, 30(2):79–116, 1998.

[17] T. Lindberg. Edge detection and ridge detection with automatic scale selection. *International Journal of Computer Vision*, 30(2):117–154, 1998.

[18] T. Hildebrand and P. Rüegsegger. A new method for the model independent assessment of thickness in threedimensional images. *J. Microsc.*, 185:6775, 1997.

[19] J. Ohser, C. Redenbach, and K. Schladitz. Mesh free estimation of the structure model index. *Image analysis and stereology*, 28(3):179–186, 2009.